Solidification of Ni-Re Peritectic Alloys

W.J. BOETTINGER, D.E. NEWBURY, N.W.M. RITCHIE, M.E. WILLIAMS,
U.R. KATTNER, E.A. LASS, K.-W. MOON, M.B. KATZ, and J.H. PEREPEZKO

Differential thermal analysis (DTA) and microstructural and microprobe measurements of DTA and as-cast Ni-Re alloys with compositions between 0.20 and 0.44 mass fraction Re provide information to resolve differences in previously published Ni-Re phase diagrams. This investigation determines that the peritectic invariant between liquid, Re-rich hexagonal close packed and Ni-rich face center cubic phases, L + HCP → FCC, occurs at 1561.1 °C ± 3.4 °C (1σ) with compositions of liquid, FCC and HCP phases of 0.283 ± 0.036, 0.436 ± 0.026, and 0.828 ± 0.037 mass fraction Re, respectively. Analysis of the microsegregation in FCC alloys yields a partition coefficient for solidification, k = 1.54 ± 0.09 (mass frac./mass frac.). A small deviation from Scheil behavior due to dendrite tip kinetics is documented in as-cast samples. No evidence of an intermetallic phase is observed.

I. INTRODUCTION

IN the continuing drive to extend the operating temperature of Ni-base superalloys, their chemistries have become increasingly complex and some alloying additions include refractory metals, such as Re. While each of the alloy additions and the level of addition have a documented effect on the superalloy performance, the analysis of the multicomponent alloy phase equilibria has required the use of computational thermodynamic methods using the CALculation of PHAse Diagrams (CALPHAD) method[1] to provide data critical in designing solidification processing and subsequent solid-state heat treatments.

A key part of the assessments that comprise the multicomponent database is the binary phase equilibria involving Ni and each of the alloy additions. From the foundation of accurate binary phase equilibria, multicomponent relationships can be calculated and refined by the addition of ternary and higher order data. Inaccuracies in the binary phase equilibria will propagate through the calculations and lead to corresponding inaccuracies in the predicted multicomponent phase relations. With the large number of components in Ni-base superalloys, it may not be clear where the origin of the inaccuracies is located so that accurate binary phase diagram assessments are essential.

The present paper resolves differences in the reported Ni-Re phase diagrams. First, existing phase diagrams are surveyed. Second, differential thermal analysis (DTA) measurements are presented on a series of Ni-Re alloys to set the peritectic temperature. Third, microprobe measurements on two-phase alloys provide an experimental determination of the face-center-cubic (FCC) and hexagonal-close-packed (HCP) phase compositions at the peritectic temperature. Microprobe results on as-cast material also determine the partition coefficient for solidification of the Ni-rich FCC phase, which when combined with the FCC composition at the peritectic temperature, gives an estimate for the liquid composition at the peritectic temperature. Finally, electron backscatter diffraction (EBSD) and transmission electron microscopy (TEM) analysis are employed to clarify crystallographic aspects of the differences in the microsegregation patterns of samples prepared by slow cooling in the DTA and by faster cooling in the as-cast material. An additional goal of the research is to check for the high-temperature existence of an intermetallic compound, Ni$_4$Re, reported at lower temperatures by atomistic calculation.[2]

II. PHASE DIAGRAM SURVEY

Due to the experimental difficulties of dealing with the high temperatures involved in the Ni-Re system, considerable variation exists in the published phase

W.J. BOETTINGER is with the Theiss Research, La Jolla, CA 92037 and also with the Materials Science and Engineering Division, National Institute of Standards and Technology, Gaithersburg, MD 20899-8555. Contact e-mail: william.boettinger@nist.gov D.E. NEWBURY and N.W.M. RITCHIE are with the Materials Measurement Science Division, National Institute of Standards and Technology. M.E. WILLIAMS, U.R. KATTNER, E.A. LASS, K.-W. MOON, and M.B. KATZ are with the Materials Science and Engineering Division, National Institute of Standards and Technology. J.H. PEREPEZKO is with the Department of Materials Science and Engineering, University of Wisconsin, Madison, WI 53706.
Manuscript submitted July 19, 2018.
Article published online November 27, 2018.

diagrams. Two versions of the Ni-Re phase diagram are available in the older literature: Reference 3 based on Reference 4 and Reference 5 based on Reference 6. The latter is reproduced in various subsequent ASM publications.[7] All show a simple peritectic type diagram between the liquid, the HCP Re solid solution (Re) and the FCC Ni solid solution (Ni), L + (Re) → (Ni). The only source of data for the peritectic temperature of 1620 °C ± 25 °C for these diagrams was obtained from Reference 8. Visual observation of melting was employed but no information was given as to how the temperature was calibrated.

Figure 1 summarizes the experimental data points obtained by References 4, 8 through 13 and the results of two thermodynamic phase diagram assessments.[13,14] The figure also includes the data points of the present paper to be described below. The more recent assessment of Yaqoob and Joubert[13] yields a lowered peritectic temperature based on their DTA measurements of 1541 °C ± 3 °C and includes the solvus data of References 10 and 11 that were not available for the assessment of Reference 14. The assessed phase diagram of Reference 13 puts the maximum solubility of Ni in the HCP Re-rich phase much higher than given in phase diagrams drawn by References 3 and 5; *viz.*, ≈ 36 pct mole fraction Ni (14 pct mass fraction Ni). The peritectic invariant points from the two assessments as well as the results of the present paper are given in Table I. The present results are in good agreement with the values presented by Reference 13.
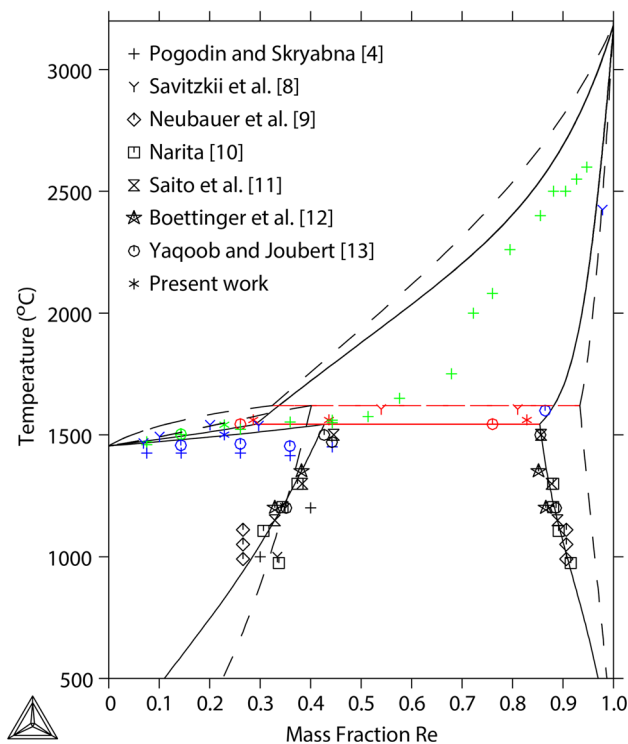

Fig. 1—Ni-Re phase diagram calculated by Huang and Chang[14] (dashed lines) and Yaqoob and Joubert[13] (solid lines). The experiment points from the literature are also shown: black = solvus, blue = solidus, green = liquidus and red = peritectic.

Other research[2] has suggested the existence of an intermetallic phase, Ni_4Re, which is isomorphous with Ni_4Mo having the $D1_a$ crystal structure that is an ordered variant of the FCC structure. They showed the Ni_4Re compound to be stable by quantum mechanical high-throughput calculations at 0 K. Monte Carlo simulations show that it is thermally persistent up to ≈ 930 K when considering configurational entropy. The experimental existence of this compound was inferred from EXAFS (Extended X-ray Absorption Fine Structure). In addition, AFLOWLIB, (Automated Flow Library)[15] also reports this phase as stable ground state. Another phase $NiRe_3$ with hexagonal $D0_{19}$ structure is also reported as stable ground state by the AFLOWLIB, OQMD (Open Quantum Materials Database)[16] and Materials Project[17] libraries. One goal of this research was to determine if the Ni_4Re phase exists near the liquidus.

The solidification of peritectic alloys has been reviewed by Kerr and Kurz.[18] Their Figure 16 shows three types of processes possible near a thermodynamic peritectic invariant $L + \alpha \rightarrow \beta$: (a) the peritectic reaction, (b) the peritectic transformation, and (c) the direct solidification of β on α. The peritectic reaction is only observed in small microstructural regions and requires liquid diffusion of solute in the small liquid groove between the growing α and β phases near the peritectic temperature. The peritectic transformation is a solid-state transformation, $\beta \rightarrow \alpha$, occurring below the peritectic temperature requiring solid-state diffusion that is important in interstitial alloys with fast solid diffusion. The direct formation of β on pre-existing α mechanism, (c), is the most important in substitutional alloys such as Ni-Re. During cooling, solidification of the high-temperature HCP phase is followed by solidification of the FCC phase forming on the pre-exiting HCP phase when the liquid composition is depleted in Re to below the peritectic liquid composition.

III. EXPERIMENTS

A. *Materials*

Five compositions were arc melted from 99.99 pct purity Ni and Re under gettered Ar: Ni-20 pct Re, − 25 pct Re, − 36 pct Re, − 42 pct Re, and − 44 pct Re for DTA and microstructural studies. An additional sample of Ni-42 pct Re was prepared by induction melting and chill casting. In all cases, complete melting was achieved. Several samples were annealed at 1500 °C. All compositions reported in this paper are given in mass percentage or mass fraction unless otherwise stated. The two lower Re compositions were selected to provide samples that solidify as single-phase FCC, while the higher Re compositions were selected to provide samples that solidify as two-phase FCC + HCP according to the phase diagram. As-cast and selected DTA samples were mounted for Scanning Electron Microscopy (SEM) Backscatter (BS) metallography and microprobe examination. The two types of samples provide a comparison of microstructure obtained at two

Table I. Summary of Thermodynamic Assessed Peritectic Invariant Temperature and Phase Compositions from Refs. [13] and [14] and Results of Present Experimental Work with One Sigma Uncertainty Estimates

Source	Temperature (°C)	Liquid (Mass Frac. Re)	FCC (Mass Frac. Re)	HCP (Mass Frac. Re)
14	1620.1	0.324	0.401	0.933
13	1543.6	0.291	0.427	0.834
Present work	1561.1 ± 3.4	0.283 ± 0.036	0.436 ± 0.026	0.828 ± 0.037

different cooling conditions. Electron Back Scatter Diffraction (EBSD) and Transmission Electron Microscopy (TEM) were performed on selected samples.

B. Measurement Procedures

1. Thermal analysis
Thermal measurements were made with Netzsch* 404

---

*Trade names are used for completeness and do not constitute an endorsement by NIST.

---

or 409 DTA instruments on 30 to 60 mg samples in alumina cups using gettered Ar flowing at 40 mL/min. Samples were heated from 1400 °C to the maximum operating temperature of the instrument, about 1670 °C at 10 °C/min and cooled at the same rate. We note that for the higher Re alloys, complete melting in the DTA could not be achieved. The instrument was calibrated using the temperature of the onset of melting of pure Ni recorded at a heating rate of 10 °C/min. The interpretation of DTA data employed the methods described in Reference 19. For the pure Ni calibration run, the observed temperature difference between onset and peak is 12 K and the difference between peak and return to baseline is 3 K. For melting of a pure metal, peak and return-to-baseline temperatures are functions only of sample mass and the heat flow within the DTA instrument. Superheating and interface kinetics for melting are negligible. Thus, for alloys with freezing ranges smaller than ≈ 15 K, only onset temperatures are useful. Peak and return-to-baseline temperatures are used for larger freezing range alloys as described in Reference 19.

2. Microprobe
Two instruments were used at 20 keV employing Ni K and Re L lines and elemental Ni and Re standards: (1) *For point measurements and line scans*—a JEOL-8500f thermal field emission gun SEM using a Bruker QUAD-SDD detector, matrix corrections with NIST DTSA II (Deneb version; multiple linear least squares fitting to experimentally measured peaks references from the elemental standards), spectrum integral: ≈ 7.5 × 10^6 counts (0.15 keV to 20 keV); (2) *For randomized pixel by pixel mapping*—a TESCAN MIRA3 tFEG-SEM with four separate 30 mm^2 PulseTorr SDD-EDS detectors at 38 mm giving a solid angle of 0.084 sr for the summed signal. The use of four detectors allowed sufficient

counts to permit full quantitative analysis on an individual pixel basis. The detectors were mounted around the optic axis of the instrument with separations of approximately 90 deg. Spectra were collected from different locations in a random order with a custom software system based upon NIST DTSA-II. Concentration uncertainty (1σ) reported is based upon measured intensities of unknown and standards propagated through the matrix corrections. Individual point measurements employed longer count times (≈ 50 seconds) and had an uncertainty of 0.1 to 0.2 pct Re. Line scan measurements employed shorter acquisition (≈ 10 seconds) times and had an uncertainty of 0.4 to 0.5 pct Re.

3. EBSD and TEM
Electron backscatter diffraction patterns were acquired with a JEOL JSM-7100 FE-SEM, 16 mm working distance, 70 deg tilt 20 kV, 2.5 nA with an Oxford NordlysNano detector. EBSD maps were constructed with AZtec software and identified the HCP and FCC phases as well as grain boundary locations. TEM samples were prepared by dimpling and ion milling and examined with a FEI Titan TEM.

IV. RESULTS

A. DTA

Figure 2(a) shows data for the Ni-25 pct Re alloy from a sample that was shaped by grinding to match the cup shape and annealed for 24 hours at 1400 °C to reduce dendritic coring from previous solidification. The first melting occurs at 1501 °C. Temperatures mentioned in the text are indicated on the figures. The peak occurs at 1526 °C. Before the return of the signal to the baseline at about 1571 °C, there is a shoulder at 1542 °C. Subsequent cooling shows two general features: an exothermic peak with an onset at 1540 °C followed by a broad peak that does not return to baseline until near the melting point of pure Ni. It is known from the microstructural analysis described below that this alloy composition solidifies as a single-phase FCC. Thus, these data are interpreted as follows. From heating data, the equilibrium solidus is taken as 1501 °C. The shoulder at 1542 °C is taken as the end of melting and thus gives an upper bound for the liquidus. From the cooling data, a lower bound on the liquidus is taken as 1540 °C. Thus, from the upper and lower bounds on the liquidus temperature obtained from the heating and cooling respectively, we conclude
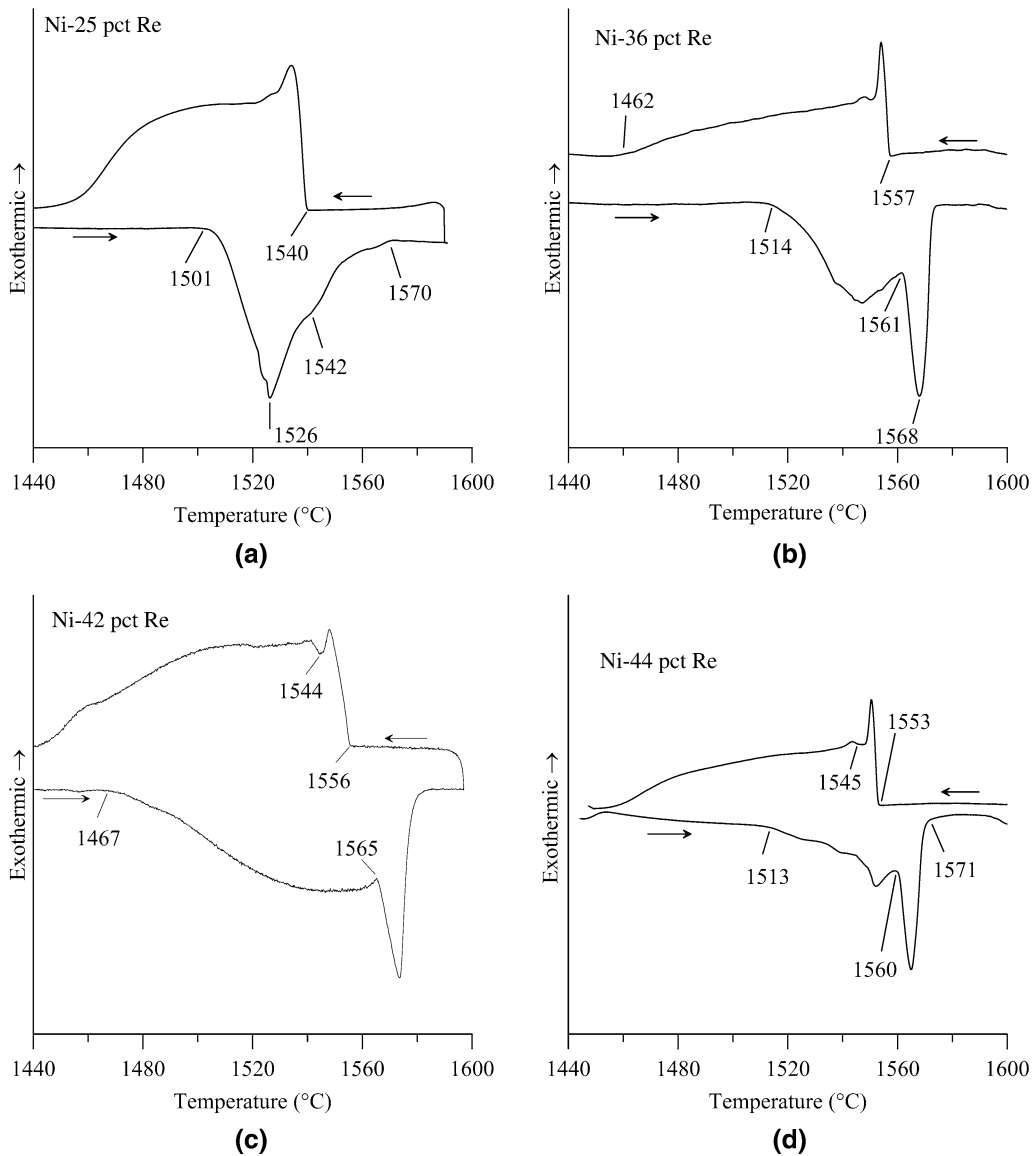
Fig. 2—DTA heating and cooling scans of Ni-Re alloys: (*a*) Ni-25 pct Re, (*b*) Ni-36 pct Re, (*c*) Ni-42 pct Re, and (*d*) Ni-44 pct Re.

that the liquidus temperature for the Ni-25 pct Re is between the two and is taken as 1541 °C. We note that the microprobe results find the average composition of this alloy to be Ni-22.9 pct Re. The broad peak following the onset of solidification is consistent with the FCC dendritic solidification microsegregation pattern observed in these samples after solidification as shown below in Figure 4(a).

For Ni-36 pct Re, the data shown in Figure 2(b) are from the second melting in the DTA to avoid erratic signals due to the shape change of the sample on first melting. As shown below in Figure 4(b), this alloy contains dendrites of HCP and FCC phases. As such, the onset of melting at 1514 °C followed by a broad endothermic hump is indicative of melting of the microsegregated FCC phase. A sharp onset follows at 1561 °C, with peak in the endotherm at 1568 °C. No

further endothermic activity is seen up to the maximum temperature achieved for this sample of 1630 °C. Subsequent cooling shows an exothermic peak with onset at 1557 °C, whose steepness indicates some supercooling for the initiation of the FCC formation. Apparently, the HCP phase does not provide a good nucleation substrate for the FCC phase. A shallow broad peak follows that does not return to baseline until ≈ 1462 °C. These data are interpreted as follows. On heating, the temperature of 1514 °C is merely the start of melting of the microsegregated solid and has no thermodynamic significance. The presence of the sharp peak beginning at 1561 °C with a total width of 13 K (comparable to melting of pure Ni) suggests an invariant reaction that we take as the peritectic temperature. However, there is no sign of a liquidus signal for the HCP phase as it is above the maximum temperature of

the DTA scan. On cooling, the steep onset at 1557 °C is due to the nucleation of FCC in the presence of the unmelted HCP phase. These data place a lower bound on the peritectic temperature. The broad exotherm not ending until 1462 °C is, like the Ni-25 pct Re alloy, caused by the dendritic freezing of the FCC phase as documented in the micrograph of the DTA sample shown in Figure 4(b).

On melting of Ni-42 pct Re and Ni-44 pct Re samples, similar sharp endothermic peaks are observed with onset temperatures of 1565 and 1560 °C respectively (Figures 2(c) and (d)). They are very close to the temperature of the onset of the peak at 1561 °C seen in the Ni-36 pct Re alloy. The onset of the peritectic reaction on cooling is 1556 and 1553 °C respectively for the two compositions. We conclude from the heating runs of the data shown in the figures plus other heating runs (not shown) that the peritectic temperature is 1561.1 °C ± 3.4 °C (n = 14). Here and elsewhere in the paper, the mean, sample standard deviation, and the number of measurements are reported. Here, n refers to the total number of DTA scans from the 36, 42, and 44 pct samples.

B. General Microstructure

The microstructure of several as-cast samples is shown in Figure 3 with backscatter images. The Ni-25 pct Re sample has no bright Re-rich phase and shows a dendritic structure of the FCC Ni phase with higher Re content at the dendrite cores and lower Re content between the cores in the last material to solidify. (This will be quantified in the microprobe results section). On the contrary, the Ni-36 pct Re, Ni-44 pct Re micrographs contain both dendrites of bright Re-rich HCP material and dendrites of gray FCC phase surrounding the Re-rich dendrites. The darkest gray is the last to solidify. Many gray FCC dendrites form within the large liquid regions between the Re-rich HCP dendrites. A larger fraction of the bright Re-rich HCP phase is evident in the Ni-44 pct Re sample than in the Ni-36 pct Re sample.

Figure 4 shows micrographs of selected DTA samples oriented as they were positioned in the DTA cup. The Ni-25 pct Re sample is like the as-cast material but with a coarser dendritic structure. In both Ni-36 pct Re and Ni-42 pct Re, the bright Re-rich HCP phase is seen at the bottom indicating that the Re-rich particles, being denser than the Ni-rich liquid, have settled due to gravity. We were unable to fully melt the samples in the DTA. Thus, Re-rich particles would have had time during the transition from heating runs to cooling runs to settle. The fact that the particles are dendritic and not rounded in character does however show that re-solidification of a significant portion of the Re phase takes place during the cooling in the DTA from ≈ 1650 °C down to the peritectic temperature. There is no sedimentation in the Ni-25 pct Re alloys because it can be completely melted in the DTA.
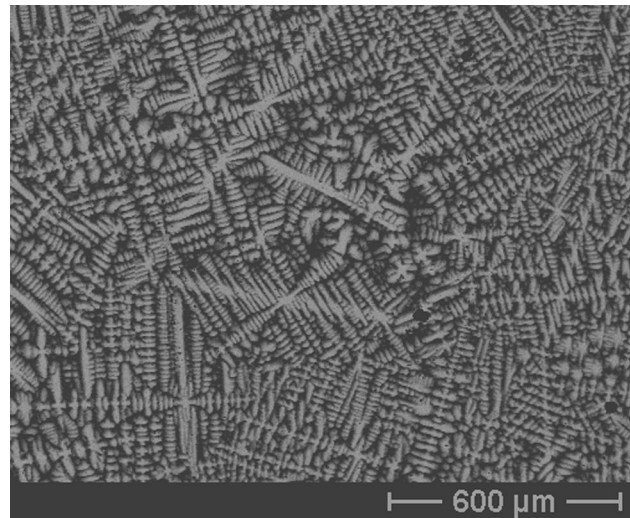
(a)
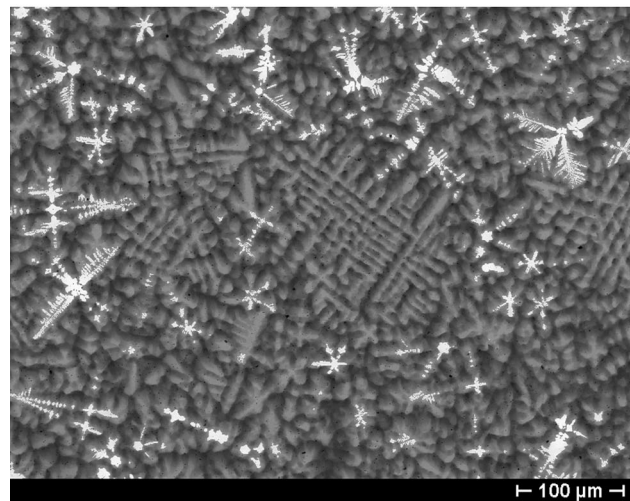
(b)
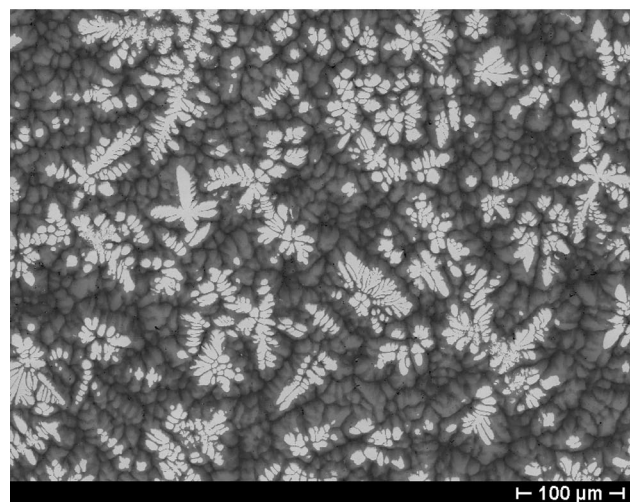
(c)

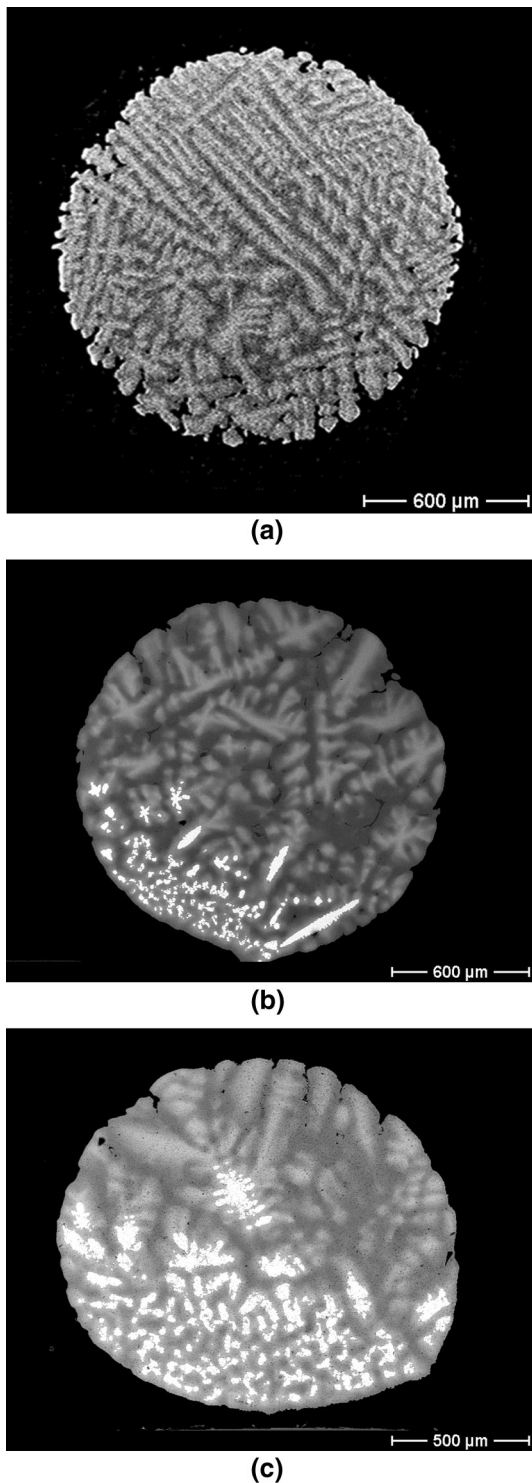Fig. 3—As-cast structures of (a) Ni-25 pct Re, (b) Ni-36 pct Re, and (c) Ni-44 pct Re.

Fig. 4—Views of DTA samples, (a) Ni-25 pct Re, (b) Ni-36 pct Re, and (c) Ni-44 pct Re.

C. EDS & EBSD Measurements

1. DTA samples

Energy dispersive X-ray spectroscopy (EDS) line scans from DTA samples crossing HCP/FCC interfaces were performed to establish the maximum Re content observed in the FCC phase and the minimum Re

content in the HCP phase. Spot mode measurements were also performed. The line scans and micrographs are shown in Figures 5(a) and (b) for the Ni-36 pct Re and Ni-42 pct Re DTA samples, respectively. The jump in composition across the interface between the bright HCP phase and the gray FCC phase is clearly shown. The maximum solubility of Re in FCC phase is ≈ 45 pct Re and the minimum level of Re in the HCP phase is ≈ 86 pct Re. In Table III presented in Section V, we summarize the mean, standard deviation and number of measurements of all the results of this paper for these two solubility limits. A single minimum in the center of the FCC profile between the Re-rich particles is observed in the DTA samples. This is classical microsegregation expected for a peritectic system for the direct solidification of β on α, in this case FCC on HCP.

2. As-cast Ni-20 pct Re and Ni-25 pct Re

Investigation of the solidification of the FCC phase was conducted on the 20 pct Re and 25 pct Re as-cast alloys using the randomized pixel by pixel EDS mapping technique. Because these alloys are single-phase FCC, there is no concern about the probe beam hitting the interface between two phases and thus obtaining erroneous phase composition values. Figures 6(a) and (b) show electron backscatter images of the 100 μm × 100 μm areas that were measured. A dendritic microstructure is evident in each with light gray Re-rich regions at the dendrite cores and dark gray Ni-rich areas between the dendrites. EDS data were collected for a 256 × 256 grid. The mean compositions of all the pixels deviated from the nominals slightly; viz., Ni-18.17 pct Re and Ni-22.85 pct Re for the 20 pct and 25 pct alloys, respectively. The individual pixel composition values were sorted from highest Re to lowest Re and numbered from 1 to 256^2. A plot of the Re values (y-axis) vs their rank number rescaled from 0 to 1 (x-axis) is shown in Figure 6(c) for Ni-20 pct Re and Ni-25 pct Re alloys. Such a procedure yields a composition vs fraction solid curve that can be compared to simple solidification microsegregation models such as a Scheil analysis. The fraction solid obtained by the rank ordering process would be area fraction of the image, which we equate to volume fraction because of the random nature of the section. The data show that the highest value for Re content observed (near zero on the x-axis) is ≈ 28 pct Re and ≈ 38 pct Re for the 20 pct Re and 25 pct Re alloys, respectively. Taking the ratio of the composition at zero fraction solid to the bulk alloy composition (the liquid composition when the core of the dendrite forms) provides a quick estimate of the partition coefficient for solidification, k, (solid composition/liquid composition); viz., 0.28/0.18 = 1.56 and 0.38/0.23 = 1.65 for the two alloys respectively.

The data in Figure 6(c) can be fit to the Scheil equation:

$$C_S = kC_0(1 - f_S)^{k-1}, \qquad [1]$$

where the average measured composition, C_0, from all the points from each curve was used as the bulk alloy composition and the partition coefficient, k, was a fitting
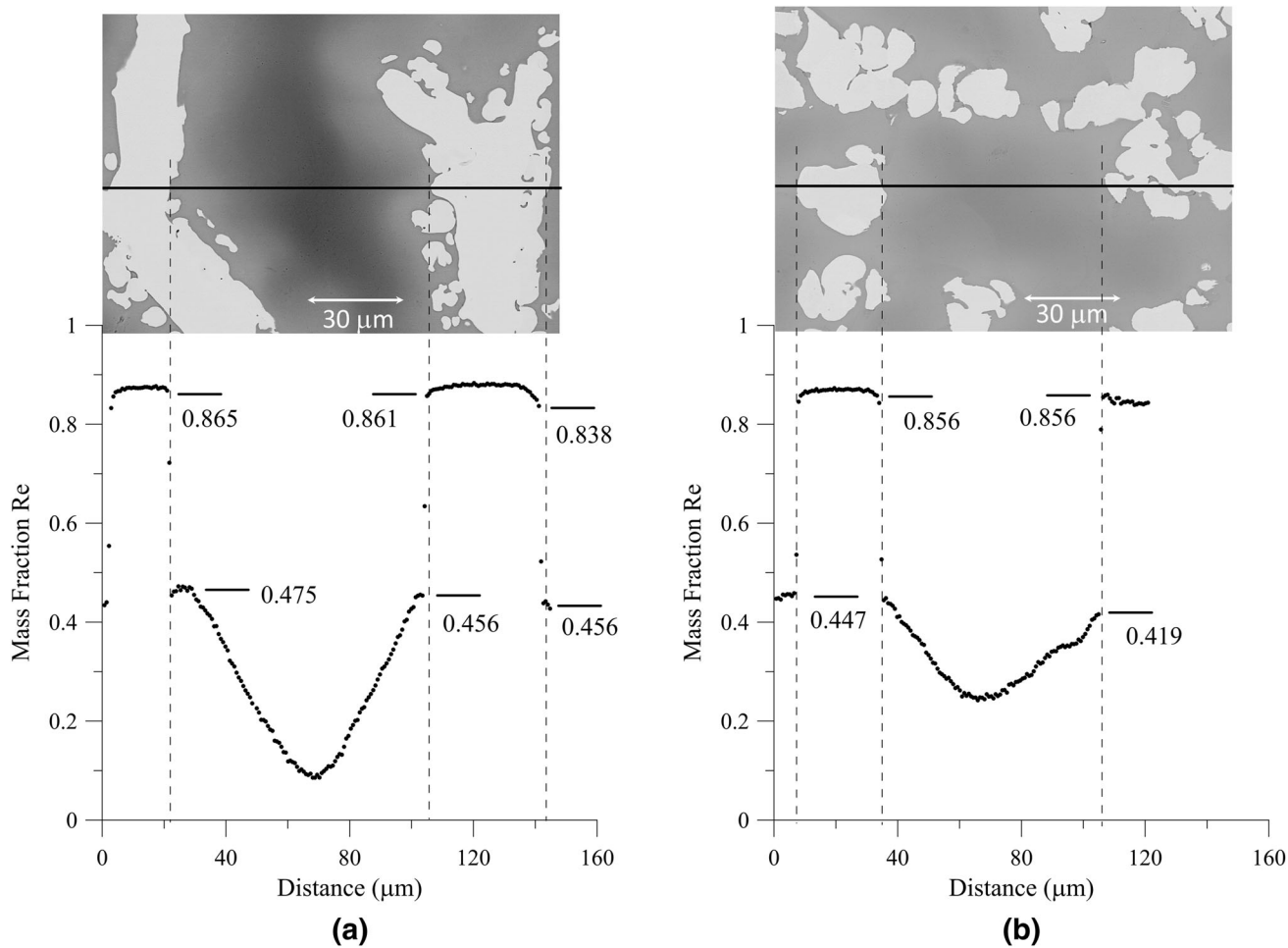
Fig. 5—Microprobe line scans from (*a*) Ni-36 pct Re DTA sample and (*b*) Ni-42 pct Re DTA samples.

parameter. The non-linear fit for the Ni-20 pct Re alloy gives a value of 1.52 whereas for Ni-25 pct Re alloy a value of 1.64 was obtained. Additional values were also obtained using linear fits to the logarithm of Eq. [1] and using additional microstructural areas of the two alloys. In summary, a mean value for $k = 1.54 \pm 0.09 \, (n = 32)$ was obtained. Technically, the fraction solid in Eq. [1] is mass fraction solid. We found a negligible difference using a conversion from volume fraction to mass fraction.

A closer look at the dendritic structures in Figures 6(a) and (b) shows rather abrupt spatial changes in contrast. Figure 7 shows EDS data extracted from the pixel by pixel data and backscatter gray scale data from a line across the dendritic structure (indicated) taken from the top of Figure 6(a). Flat profiles across the dendrite cores are evident with rather abrupt drops in composition between the dendrite cores. Figure 8(a) shows a backscatter image while Figure 8(b) shows a EBSD "all Euler angle" color map showing the grain misorientation within the dendritic structure. All backscattered electron diffraction patterns were indexed as being FCC. Many of the abrupt contrast changes in Figure 8(a) are seen to lie within single grains, but some occur at grain boundaries. This will be discussed in more detail in the Section V and "Appendix B".

### 3. As-cast Ni-36 pct Re and Ni-42 pct Re

The pixel by pixel technique was not used for the two-phase alloys because the microprobe beam would hit the interface between the HCP phase and the FCC phase giving a false sense of the microsegregation. Instead point measurements and line scans are reported. Point analysis results for a Ni-42 pct Re as-cast sample is shown in Figure 9 and Table II. Similar results were obtained from the Ni-36 pct Re as-cast alloy. The backscattered SEM image shows a microstructure with bright Re-rich HCP particles with a gray FCC region between the Re particles. (The structure of these regions is established by EBSD below) The locations of the analysis points are labeled in the BS image and Re values are given below the micrograph ordered by increasing Re content. The bright phase is high in Re content with values between 80 and 83 pct. The gray FCC phase has significant variations in Re content as the contrast ranges from light gray to dark gray. The light gray FCC material typically surrounds the bright Re-rich particles; but in other places the light gray FCC material is not in contact with the bright Re-rich HCP particles. The dark gray FCC material is found surrounding the light gray material. Microprobe analysis positions were chosen for the lightest gray and the

(a)

(b)

(c)
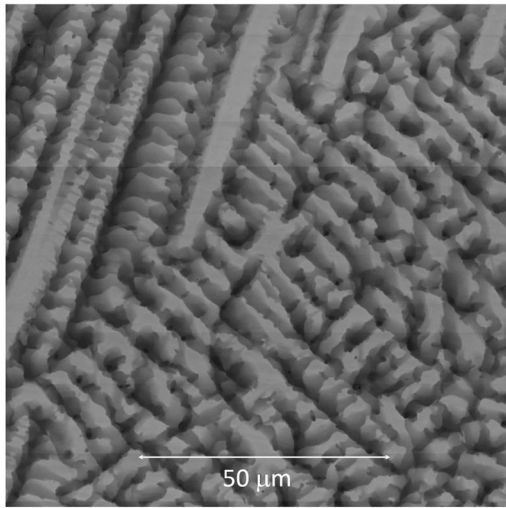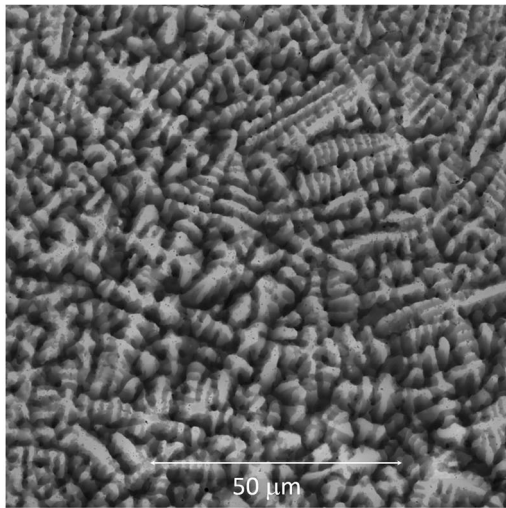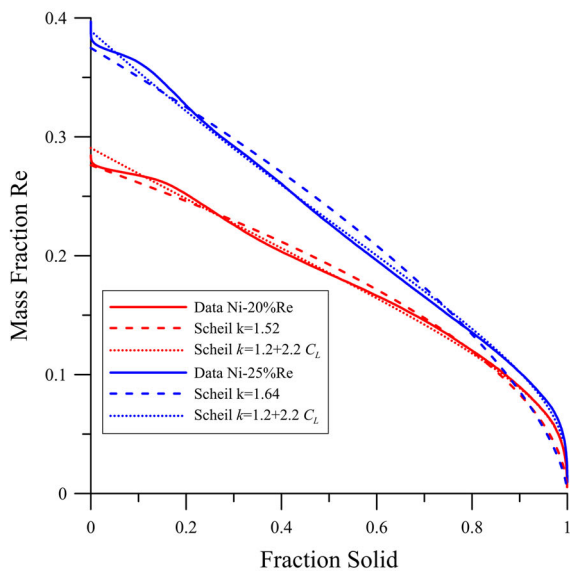
Fig. 6—As-cast microstructure of single-phase FCC alloys: (a) Ni-20 pct Re, (b) Ni-25 pct Re, and (c): randomized pixel composition measurements on (100 μm × 100 μm) areas shown in (a) and (b) sorted from highest to lowest Re content. Also shown are best fits to the Scheil model using the measured average compositions of 18.2 pct Re and 22.9 pct Re and using partition coefficients of 1.52 and 1.64, red and blue respectively. Also shown are fits for the two alloys using a composition-dependent partition coefficient as described in "Appendix A".
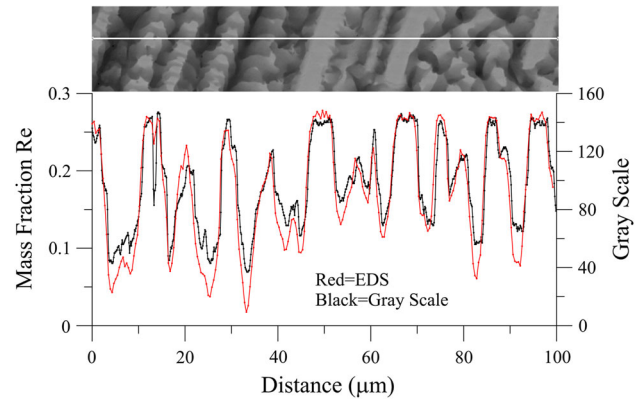

Fig. 7—EDS and backscatter image gray scale line scans across dendritic structure of the top part of Fig. 6(a).

darkest gray regions. The highest composition of the light gray regions is 42.05 pct Re and the lowest composition in the dark gray regions is 5.34 pct Re. Taken alone, the light gray and dark gray regions almost appear as separate phases. However, the boundary between light and dark gray is quite wavy and gossamer.

Examples of line scans with corresponding backscatter SEM images for Ni-36 pct Re and Ni-42 pct Re as-cast samples are shown in Figures 10(a) and (b). The line scans cross from bright Re-rich HCP particles and into the Ni-rich material. From the jumps in composition across the FCC/ HCP interface in these figures and other line scans not shown, the compositions of the FCC and HCP at the peritectic invariant from the as-cast samples are ≈ 43 pct Re and ≈ 82 pct Re. The scatter in these measurements is significant and is documented in Table III in Sections V and VI, where the mean, standard deviation of all the results of this paper for these two numbers are given.

Also of note in Figure 10 is the variation of Re content in the FCC material between the HCP dendrites corresponding to the light gray and dark gray material in the backscatter images. These variations, although relatively abrupt, appear to be continuous in the line scans. These abrupt variations in contrast are not present in the DTA samples (Figure 5) where a single minimum in Re content is observed between each pair of Re particles. The latter is characteristic of the formation of β on α mechanism described for peritectic alloys by Reference 18. In the as-cast samples, the microsegregation in the FCC gray phase between each pair of HCP Re particles contains rapid spatial changes from light to dark gray indicating dendritic growth of the FCC
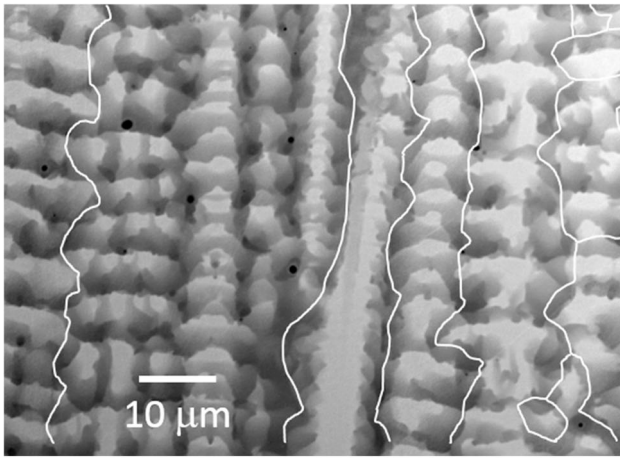
(a)
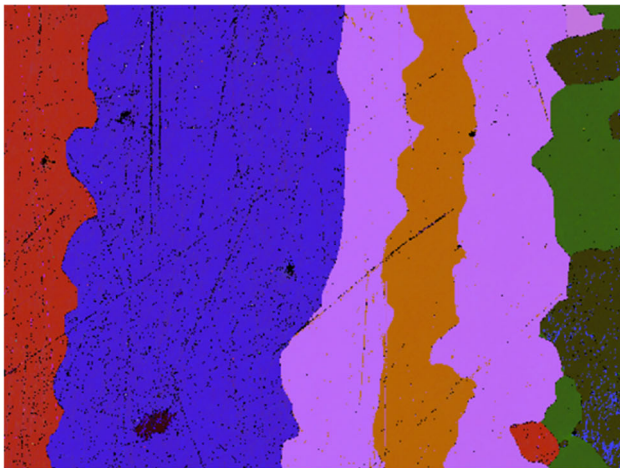
(b)

Fig. 8—(*a*) Backscatter image and (*b*) EBSD colored "all Euler angle" map of Ni-20 pct Re as-cast alloy. Location of grain boundaries are overlaid in the BS image as white lines.
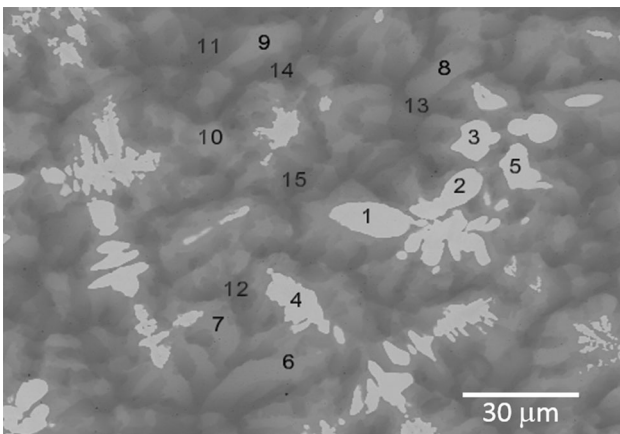

Fig. 9—Microstructure of as-cast Ni-42 pct Re sample with locations used for spot mode microprobe measurements given in Table II.

between the HCP particles. Similar abrupt contrast changes are seen in the FCC dendritic structures of Figures 6(a) and (b).

Table II. Spot Mode Microprobe Data from Locations Indicated in Fig. 9, Sorted from Lowest to Highest Fraction Re

Location	Contrast	Re Mass-Fraction
11	dark gray	0.0534 ± 0.0008
15	dark gray	0.0756 ± 0.0009
13	dark gray	0.0871 ± 0.0009
14	dark gray	0.0924 ± 0.0009
12	dark gray	0.1509 ± 0.0011
6	light gray	0.3901 ± 0.0015
8	light gray	0.3958 ± 0.0015
7	light gray	0.4036 ± 0.0015
9	light gray	0.4204 ± 0.0016
10	light gray	0.4205 ± 0.0016
4	white	0.7981 ± 0.0022
1	white	0.8198 ± 0.0022
5	white	0.8229 ± 0.0022
2	white	0.8274 ± 0.0022
3	white	0.8311 ± 0.0023

Figure 11 shows the result of examination of the structure of the Ni-42 pct Re as-cast structure obtained using EBSD. The bright Re-rich particles seen in the backscattered SEM image (Figure 11(a)) were clearly indexed as HCP in Figure 11(b) (yellow). Both light and dark gray material seen in the backscattered SEM image (Figure 11(a)) were clearly indexed as FCC in Figure 11(b) (blue). Figure 11(c) is an EBSD "all Euler angle" color map showing the grain misorientation. Some of the boundaries between light and dark gray within the FCC dendritic material correspond to grain boundaries. But a very large grain of FCC surrounds one HCP dendrite with no grain boundaries corresponding to the location of the contrast change in Figure 11(a). Thus, locations of abrupt contrast change are in some places the location of grain boundaries within the FCC dendritic material and in other places the contrast change occurs within a single grain. Similar observation was made for the Ni-20 pct Re and Ni-25 pct Re as-cast materials shown in Figure 8.

Because EBSD is not generally capable of distinguishing between disordered FCC and chemically ordered variants of FCC, and because of the report of the intermediate phase, Ni_4Re,[2] TEM and scanning transmission electron microscopy (STEM) examination was performed to determine the nature of the difference between the higher Re and lower Re regions within the interdendritic material. Figure 12(a) shows a high angle annular dark field (HAADF) image of three regions, a brightest intensity high-Re region marked as A, adjacent Ni-Re region showing mottled intensity marked as B and a gray contrast region highest in Ni marked as C. HAADF contrast is derived from the magnitude of inelastic scattering; for a given cross section (film thickness), brightness goes as atomic number to a power between 1.7 and 2. SADP (selected area diffraction pattern) from ≈ 500 nm diameter regions from the B and C regions are shown in Figure 12(b) and (c).
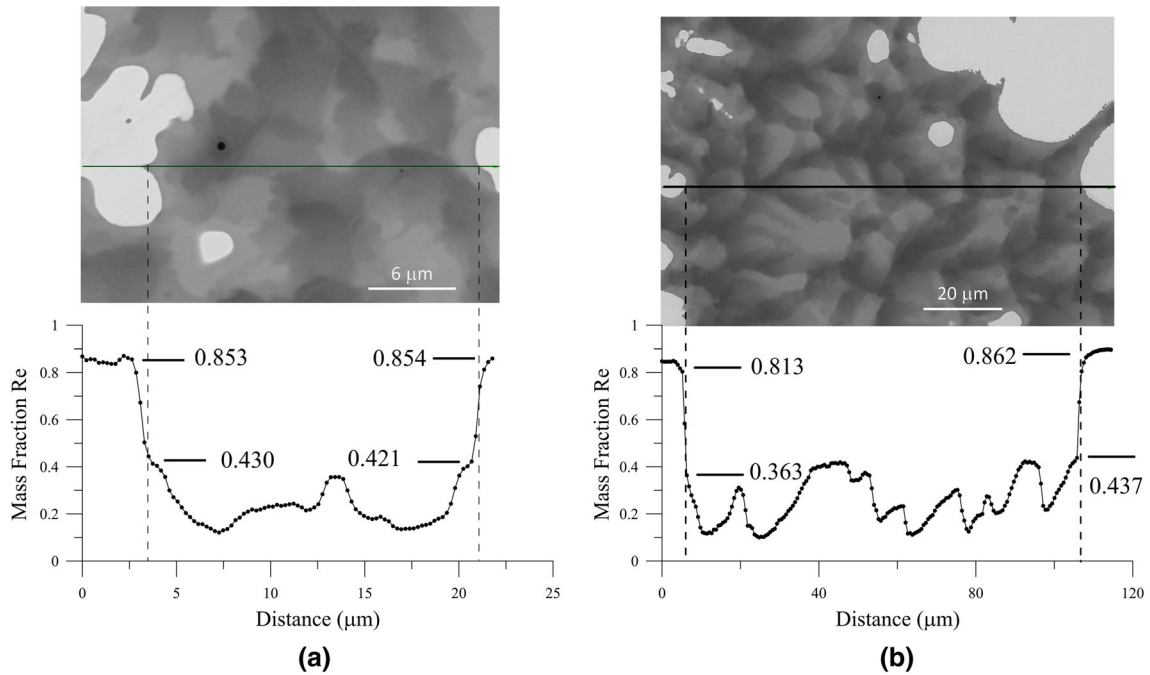
Fig. 10—As-cast microstructure and EDS line scan: (a) Ni-36 pct Re, (b) Ni 42 pct Re.

Table III. Summary of Measured FCC and HCP Phase Compositions Near the Peritectic Temperature

Sample	FCC (Mass Pct Re)	HCP (Mass Pct Re)
DTA	44.6 ± 1.8 (n = 15)	85.3 ± 1.0 (n = 17)
As-cast	43.4 ± 2.8 (n = 33)	81.9 ± 4.1 (n = 33)
Annealed	42.5 ± 3.1 (n = 4)	80.8 ± 3.7 (n = 6)
Combined	43.6 ± 2.6 (n = 52)	82.8 ± 3.7 (n = 56)

Diffraction from a featureless Ni region (C) shows only FCC diffraction spots (Figure 12(c)). Based on intensity of reflections and apparent overlap of some reflections, diffraction from the mottled region (B) strongly suggests coexistence of FCC and HCP phases in the $(111)_{FCC}/\{0001\}_{HCP}$ orientation; other HCP variants of the same orientation relationship have much less clear contribution to the diffraction pattern. Observation of other zone axis patterns are consistent with this finding. No evidence was found for the existence of a chemically ordered variant of FCC, such as $L1_2$ or $D1_a$.

Figure 13 shows a higher magnification HAADF STEM image of the mottled Ni-Re region in the FCC [110] orientation. The structure consists of connected Re-rich rod-like particles embedded in a Re-poor matrix as indicated by the brightness levels of this Z-sensitive contrast. The very fine inter-rod spacing of ≈ 20 nm indicates that this structure is a result of solid-state transformation after solidification. Due to the retrograde nature of the FCC solvus curve, considerable supersaturation occurs during solid-state cooling that would naturally lead to the formation of the HCP phase precipitates within the FCC material formed by solidification.

4. Annealed samples

Figure 14 shows the microstructure of a sample annealed in the DTA instrument to obtain the best temperature control. To avoid incipient melting of the as-cast structure, a two-step heat treatment was employed: 2 hours at 1400 °C followed by 4 hours at 1500 °C. The structure consists of bright HCP Re phase and a uniform gray FCC matrix. The dendritic contrast in the FCC material between the HCP particles that was seen in the as-cast samples is absent. The compositions of the HCP and FCC phases are 84 pct Re and 43 pct Re. These values and those from other line scans are summarized in Table III.

V. DISCUSSION

A. Phase Diagram

Summarizing the onset temperatures obtained from Figure 2 and other DTA heating scans, the temperature of the peritectic invariant L + HCP → FCC is 1561.1 °C ± 3.4 °C (n = 14) where n is the number of measurements. A randomized pixel by pixel EDS technique has been used to obtain full quantitative composition measurements from 256 x 256 arrays of points from as-cast FCC dendritic samples. Using the assumption that the solidification follows a Scheil model, the partition coefficient for solidification of the FCC phase is 1.54 ± 0.09 (n = 32).

Considerable scatter exists for the composition of the FCC and HCP at the peritectic temperature as obtained by EDS measurement of DTA, as-cast alloys and from heat-treated samples annealed close to the peritectic temperature. The summary of means, standard deviations, and number of measurements determined from
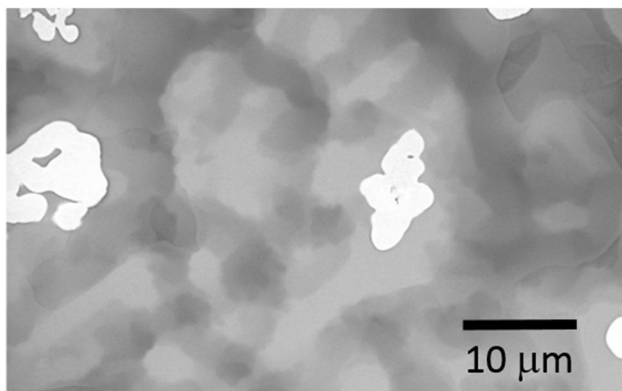
(a)

(b)

(c)

Fig. 11—Ni-42 pct Re as cast structure. (*a*) Backscattered image, (*b*) EBSD phase map (blue = FCC and yellow = HCP), and (*c*) Euler angle map showing large FCC grain (dark blue) surrounding HCP dendrite despite light gray dark gray contrast seen in (a).

line scans is given in Table III for the three types of samples. The scatter is much larger than that expected from the EDS measurement alone and may be due to the subjectivity of extracting interface compositions from line scans. We see no consistent explanation for the slightly different results obtained from the three types of samples and thus combined values are thought to be most reliable.

An estimate for the liquid composition of the peritectic reaction can now be obtained. Taking the Re content of the FCC phase at the peritectic invariant of 43.6 pct ± 2.6 pct Re and using the obtained partition coefficient of 1.54 ± 0.09, we compute the liquid composition corresponding to the first solidification of FCC by dividing the solid composition of FCC by the partition coefficients to obtain a value of 28.3 pct ± 3.6 pct. This value agrees with the fact that the 20 pct Re and 25 pct Re alloys freeze as single-phase FCC while the 36 pct Re, 42 pct Re and 44 pct Re alloys freeze with HCP followed by FCC. This value for the liquid composition is given in Table I.

Assuming a straight line liquidus for the FCC phase, the above estimate puts the liquidus slope, m_L, as $(1561 - 1455)/28.3 = 3.7$ °C/pct (mass). This converts to approximately 9.6 °C/pct (mole). From Eq. 11.41 in Reference 20, a relation between the liquidus slope and partition coefficient for a dilute alloy can be obtained as

$$\frac{m_L}{k - 1} = \frac{RT_M^2}{L_m},\qquad [2]$$

where R is the gas constant, T_M is the pure solvent melting point and L_m is the heat of fusion per mole. A partition coefficient as a mass fraction ratio of 1.54 converts to an atomic fraction ratio of approximately 1.65. Using a value for $T_M = 1728$ K and L_m of 17.48 kJ/mole,[21] the value of m_L is computed as 9.2 °C/pct (mole) in reasonable agreement with the experimental number of 9.6 °C/pct (mole).

We note that a somewhat better fit to the microsegregation profile is obtained using a composition dependent partition coefficient. Solution to the Scheil model for such a case is given in "Appendix A." The improved fits are shown in Figure 6(c) for $k = 1.2 + 2.2C_L$, where C_L is in mass fraction. This suggests that the liquidus and solidus diverge more rapidly than straight lines as the Re composition increases. Such a divergence would be expected when a metastable miscibility gap exists in the FCC phase as seen in Figure 10 of Reference 22. Indeed, the assessment of Reference 13 contains a positive heat of mixing for the FCC phase. However, this result might be putting too much faith in the accuracy of the Scheil model. A full thermodynamic (CALPHAD) treatment adding our data is beyond the scope of this paper. Such an assessment must reconcile the positive heat of mixing for the FCC in Reference 13 with the ordering predicted from atomistic calculations at 0 K.

B. Microsegregation Patterns in FCC Ni-20 pct Re and Ni-25 pct Re

Although the microsegregation data for the as-cast Ni-20 pct Re and Ni-25 pct Re are reasonably fit by the Scheil model there is a noticeable deviation. Between fraction solid of 0 and 0.1 in Figure 6(c), the measured data are seen to be flatter than the Scheil prediction. These data correspond to the dendrite core flat profiles seen in Figure 7. This deviation is most clearly seen in the histogram of the experimental data shown in Figure B1 in "Appendix B," where a peak in the histogram is evident at the highest Re content. The histogram for an alloy obeying the Scheil equation (constant k) is shown for comparison.

Deviation from Scheil behavior is expected at elevated solidification velocity as in arc and chill casting due to the details of dendrite tip kinetics as described in
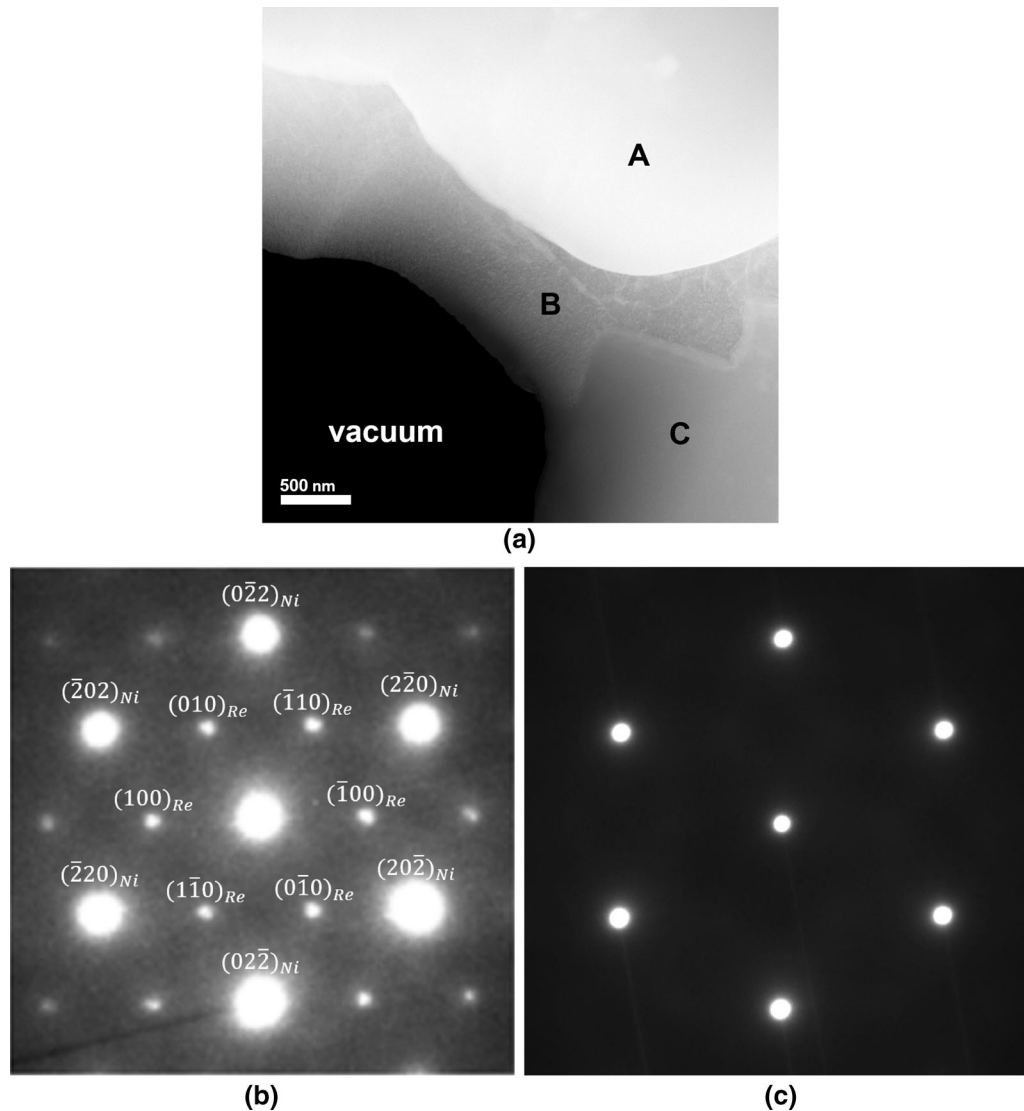
Fig. 12—(*a*) HAADF TEM image of as-cast Ni-42 pct Re alloy showing (A) Re-rich HCP dendrite, (B) intermediate Re content mottled region and (C) featureless FCC region. Brightness indicates average atomic number. (*b*) SADP from mottled region shows single orientation of FCC and multiple orientations of HCP particles in $(111)_{FCC}/(0001)_{HCP}$ orientation relation. (*c*) SADP from featureless region showing single-phase FCC.

"Appendix C." When combined with a truncated Scheil model, a relatively flat region of the microsegregation curve is expected. It is also possible that secondary dendrite arms form at high rate and possess the same flat profile in their cores. This provides a possible mechanism for much of the abrupt contrast changes seen in Figures 6(a) and (b).

C. *Microsegregation Patterns in Ni-36 Pct Re and Ni-42 Pct Re*

The microsegregation pattern observed in DTA samples agrees in general with that expected for a hyper-peritectic alloy involving substitution solid solution where solid diffusion is relatively slow; *i.e.*, direct solidification of FCC on HCP. Solidification of the high-temperature HCP phase is followed by solidification of the FCC phase during cooling when the liquid

composition is depleted in Re to below the liquid peritectic composition. Solidification of the FCC phase proceeds from the preexisting HCP particles and finishes at the centers between the particles. The composition profile has a minimum composition approaching pure Ni in the center between the Re-rich HCP particles. The solid-state transformation of the HCP to FCC is prevented by the slow solid diffusion rate.

However, the as-cast samples, Figure 10, have a more complex microsegregation pattern in the FCC phase than the DTA samples. It appears that the FCC phase between the Re dendrites solidifies by an independent dendritic process. Indeed, to a first approximation the FCC microstructure shows a classical dendritic coring pattern with high and low Re regions. What is unusual is the fact the coring pattern appears to have relatively abrupt compositional changes. Some of these changes occur at grain boundaries within the FCC phase, but
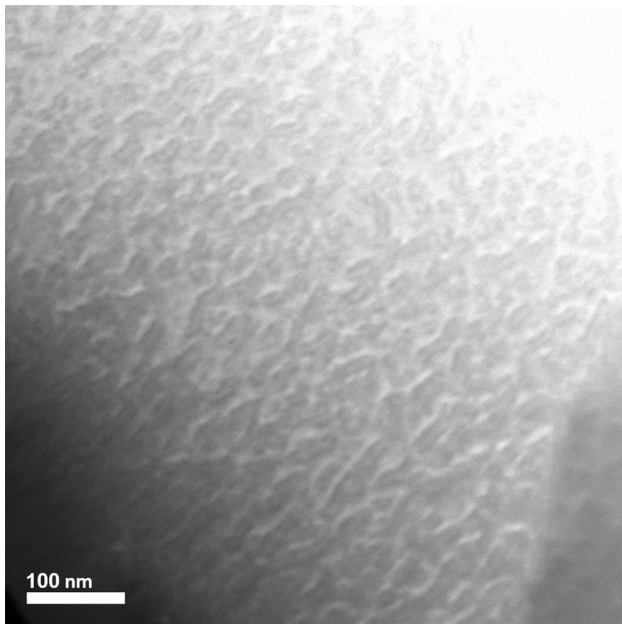
Fig. 13—HAADF STEM image from mottled region in Fig. 12 showing fine rod-like Re-rich particles (light) embedded in a Ni-rich matrix (dark).

others lie within FCC single grains. The TEM analysis suggests that these boundaries between high and low Re separate regions with and without fine Re precipitates. The presence of fine precipitates, likely by solid-state transformation during cooling, is consistent with the higher Re contents and the retrograde nature of the FCC solvus.

We propose two mechanisms that may cause the abrupt compositional changes in the FCC as-cast material. For alloys like Ni-20 pct Re and Ni-25 pct Re, it has been shown in "Appendix C" that the dendrite cores may have a uniform composition due to dendrite tip kinetics. Similar features would be expected in the dendritic structures between the Re-rich HCP phase because that process seems to occur independently of the HCP formation. A second mechanism might be dendritic fragmentation of secondary dendrite arms that melt off and form growth centers for solidification of grains with different orientations and their own dendritic growth microsegregation pattern. Impingement of these growing grains could cause some of the abrupt composition changes.

Other possible mechanisms for the formation of the abrupt composition changes within the FCC phase in the Ni-36 pct Re and Ni-42 pct Re alloy were considered and dismissed as unlikely; *viz.*, (a) peritectic transformation and (b) the existence of a cascade of two peritectic reactions, for example L + (Re) → Ni$_4$Re followed by L + Ni$_4$Re → (Ni) at lower temperature.

For the peritectic transformation, solid-state diffusional transformation of HCP to FCC would be required. For such a transformation, the diffusion of Re from the HCP phase into the FCC phase would be governed by the diffusion rates and the interface compositions of the FCC and HCP phases that would
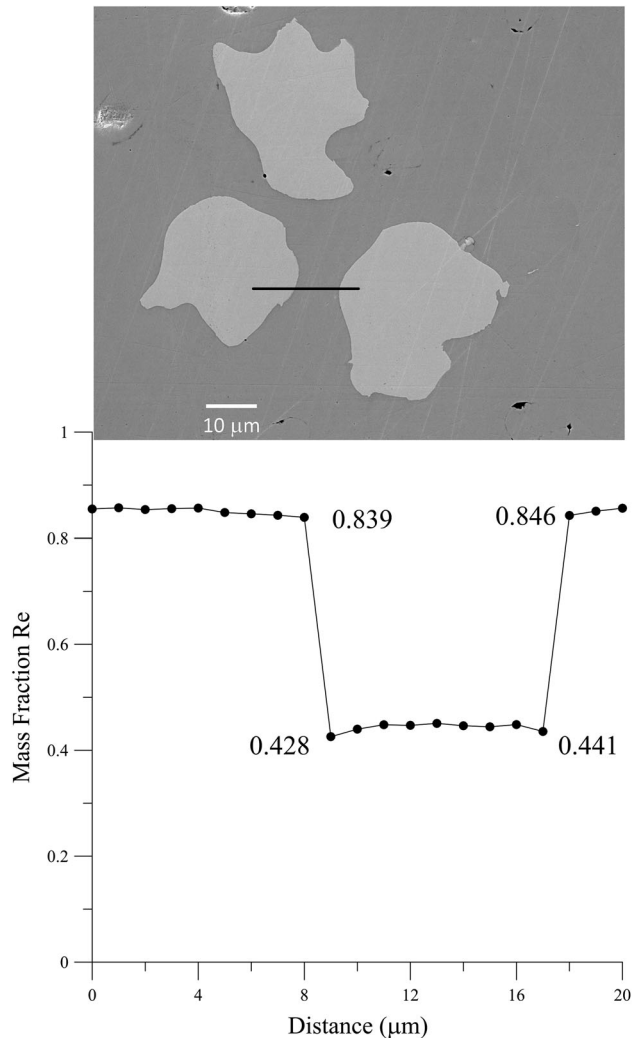

Fig. 14—Ni-42 pct Re cast sample that has been annealed in the DTA at 1400 °C for 2 h followed by 1500 °C for 4 h. The variations in contrast in the FCC phase between Re particles have disappeared. Line scan data taken at the position of the dark line are shown.

follow the two boundaries of the FCC + HCP two-phase region of the phase diagram during cooling. Such a process might produce a plateau of composition in the FCC phase for the HCP phase that is transformed to FCC in the solid state. Modeling of the peritectic transformation using the DICTRA software (DIffusion-Controlled TRAnsformations),[23] using estimated diffusion data, shows very little peritectic transformation during solid-state cooling at rates expected in arc melting or chill casting.

The measured composition of the first FCC to form is very close to the Ni$_4$Re composition thought to be a stable D1$_a$ phase by atomistic modeling below the predicted maximum stability temperature of ≈ 657 °C in this system.[2] Its presence as a solidification product would require the Ni$_4$Re phase to exist above the melting temperature of pure Ni. TEM examination present herein finds no evidence for a D1$_a$ phase or any other FCC-based ordered structure. Further, no double peritectic signal has been seen in DTA measurements.

We have found it impossible to construct a phase diagram with a cascade of two peritectics that was consistent with all the data. It should be noted that no intermediate phase has been found in diffusion couple experiments between Ni and Re at the highest temperatures studied between 990 °C and 1100 °C[9] and 1200 °C and 1350 °C.[12] Thus, the cascading peritectic idea appears to be an unlikely explanation.

VI. CONCLUSIONS

1. The peritectic temperature is 1561.1 °C ± 3.4 °C (1σ).
2. The composition of the FCC phase at the peritectic temperature is 43.6 pct ± 2.6 pct Re (mass fraction).
3. The composition of the HCP phase at the peritectic temperature is 82.8 pct ± 3.7 pct Re (mass fraction).
4. The partition coefficient for the solidification of the FCC phase using Re as the solute is 1.54 ± 0.09 (mass fraction/mass fraction).
5. Using this partition coefficient, the composition of the liquid at the peritectic reaction temperature is estimated as 28.3 pct ± 3.6 pct Re (mass fraction).
6. The solidus temperature for the Ni-25 pct Re mass fraction alloy (22.9 pct Re by microprobe) is 1501 °C. The liquidus temperature of Ni-25 pct Re mass fraction alloy (22.9 pct Re by microprobe) is 1541 °C.
7. Little data have been obtained for the HCP liquidus. For the Ni-36 pct Re alloy, a lower bound for the liquidus temperature of the HCP is 1630 °C, the maximum temperature of the scan.
8. Peritectic solidification of the more slowly cooled DTA samples follows the mechanism of solidification of FCC on preexisting HCP. Whereas in the as-cast material, independent dendritic growth of the FCC phase also is observed between the HCP phase particles.
9. The abrupt composition changes observed in the FCC phase microsegregation profiles in as-cast samples are thought to be due to dendrite tip kinetics.

ACKNOWLEDGMENTS

APPENDICES

Appendix A: Scheil for Composition Dependent Partition Coefficient

The Scheil equation in differential form is

$$\frac{df_S}{1 - f_S} = \frac{dC_L}{(C_L - C_S)}. \quad [\text{A1}]$$

For $C_S = (k_0 + k_1 C_L)C_L$, integration by partial fractions gives

$$C_L(f_S) = \frac{C_0(1 - k_0)(1 - f_S)^{k_o - 1}}{1 - k_0 - k_1\left(1 - (1 - f_S)^{k_0 - 1}\right)}, \quad [\text{A2}]$$

where $C_L = C_0$ for $f_S = 0$ has been used. An expression for $C_S(f_S)$ is obtained as

$$C_S(f_S) = [k_0 + k_1 C_L(f_S)]C_L(f_S). \quad [\text{A3}]$$

Appendix B: Histogram (Probability Density Plot) for Microsegregation

The data obtained from the pixel by pixel EDS measurement technique can be used to construct a probability density plot, $P(C_S)\Delta C_S$, which is the fraction of pixels with composition between C_S and $C_S + \Delta C_S$. It is the probability that upon selecting a random location in the microstructure that the composition will lie between C_S and $C_S + \Delta C_S$. Such a plot (Figure B1) gives a more sensitive measure of the microsegregation than Figure 6(c).

For microsegregation following the Scheil expression for constant k,

$$C_S = kC_0(1 - f_S)^{k-1} \quad [\text{B1}]$$

or

$$1 - f_S = \left(\frac{C_S}{kC_0}\right)^{\frac{1}{k-1}}, \quad [\text{B2}]$$

$P(C_S)$ is given by $-\frac{df_S}{dC_S}$. Thus

$$P(C_S)\Delta C_S = -\frac{df_S}{dC_S}\Delta C_S = \frac{1}{k(k-1)C_0}\left(\frac{C_S}{kC_0}\right)^{\frac{2-k}{k-1}}\Delta C_S. \quad [\text{B3}]$$

Figure B1 shows the experiment probability plot for the Ni-20 pct Re as-cast materials and the corresponding Scheil histogram ($C_0 = 0.1816$, $k = 1.54$). The deviation from the Scheil prediction is evident. A large
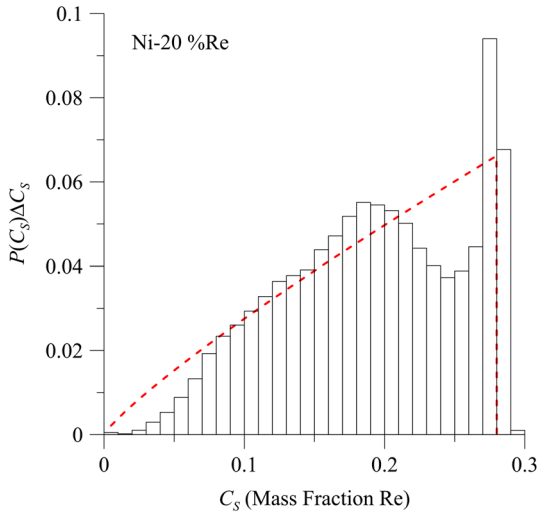
Fig. B1—Fraction of pixels $P(C_S)\Delta C_S$ measured with composition between C_S and $C_S + \Delta C_S$ for the Ni-20 pct Re as-cast alloy ($\Delta C_S = 0.01$ mass fraction Re). Dashed red line shows Scheil behavior for $k = 1.54$.

fraction of the sample, $\approx$ 15 pct of the pixels, have a narrow range of composition between 27 pct Re and 29 pct Re. This peak corresponds to the dendrite stalk and arm cores formed during fast solidification. The minimum near 25 pct Re leads to the observed abrupt change in backscatter contrast in images of the FCC dendritic structures in as-cast samples.

Appendix C: Dendrite Tip and Truncated Scheil

In the Scheil approach, the transport of solute in the liquid phase is assumed to be sufficiently rapid that the liquid can be treated as being uniform in composition at each temperature during cooling. First solidification begins at the dendrite tip. The diffusion in the liquid in front of each dendrite tip leads to the fact that solidification starts slightly below the liquidus temperature and with composition different than kC_0. Indeed the phase field method was used[24] to show the existence of relatively flat microsegregation profiles at the start of rapid dendritic solidification (See their Figure 12).

A simpler approach is given here. For a treatment of the kinetics of the dendrite tip in an alloy, the Ivantsov solution is obtained to determine the composition of solute at the dendrite tip. The marginal stability criterion is applied to determine the tip radius. The equations that govern the dendritic growth of binary alloy, C_0, at velocity, V, and temperature gradient, G, are now summarized.[25] The composition of liquid at the dendrite tip, C_L^*, is given in terms of the Péclet Number, $P = VR/2D$; by

$$C_L^* = \frac{C_0}{1 - (1-k)Iv(P)}, \quad [C1]$$

where R is the dendrite tip radius, k, is the partition coefficient, D is the liquid diffusion coefficient, and $Iv(P) = P\exp(P)E_1(P)$, where $E_1(P)$ is the first exponential integral. The tip radius is given by

$$R = 2\pi \left[\frac{T_M \Gamma}{m_L G_C \xi - G} \right]^{1/2}, \quad [C2]$$

where $T_M \Gamma$ is the capillary constant and m_L is the liquidus slope. T_M is pure material melting point and Γ is the ratio of the liquid-solid surface energy and the enthalpy of fusion per unit volume. The parameter ξ is a small correction for large P given by

$$\xi = 1 + \frac{2k}{1 - 2k - \left(1 + \left(\frac{2\pi}{P}\right)^2\right)^{1/2}}. \quad [C3]$$

The composition gradient in the liquid at the dendritic tip G_C^* is obtained from the Ivanstov diffusion solution as

$$G_C^* = -\frac{2P(1-k)}{R} C_L^*. \quad [C4]$$

The tip temperature is then given by

$$T^* = T_M + m_L C_L^* - T_M \Gamma / 2R, \quad [C5]$$

where m_L is the liquid slope. For small temperature gradient, the dendrite tip temperature approaches the liquidus temperature as the dendrite tip velocity approaches zero. With increasing dendrite tip velocity, the dendrite tip temperature drops below the liquidus. Thus, first solidification occurs at a temperature below the liquidus.

The simplest approach to couple the dendrite tip analysis to the remainder of the solidification path is called the "Truncated Scheil" method originally proposed by Flood and Hunt[26] and modified to conserve solute by Boettinger.[25] First, the dendrite operating point (tip temperature and tip liquid composition neglecting curvature undercooling) is determined as described above. Second, a solute balance is performed using the liquid and solid compositions at the tip to determine the fraction of solid formed at the tip as

$$C_L^*(1 - f_S^{tip}) + kC_L^* f_S^{tip} = C_0 \quad [C6]$$

$$f_S^{tip} = \frac{C_L^{tip} - C_0}{C_L^{tip}(1-k)}. \quad [C7]$$

Third, a Scheil calculation is performed for the remainder of the solidification path. The calculation for this last step of the procedure would be started with "initial" values for the liquid compositions equal to the tip liquid composition and the fraction of solid equal to f_S^{tip}.

In summary,

$$C_S(f_S) = \begin{cases} kC_L^* & 0 \le f_S < f_S^{tip} \\ kC_L^* \left[\frac{1-f_S}{1-f_S^{tip}}\right]^{k-1} & f_S^{tip} \le f_S < 1 \end{cases}. \quad [C8]$$

Figure C1 shows three plots (a) dendrite tip solid composition vs dendrite tip velocity, (b) fraction solid at the tip vs velocity and (c) the microsegregation profile,
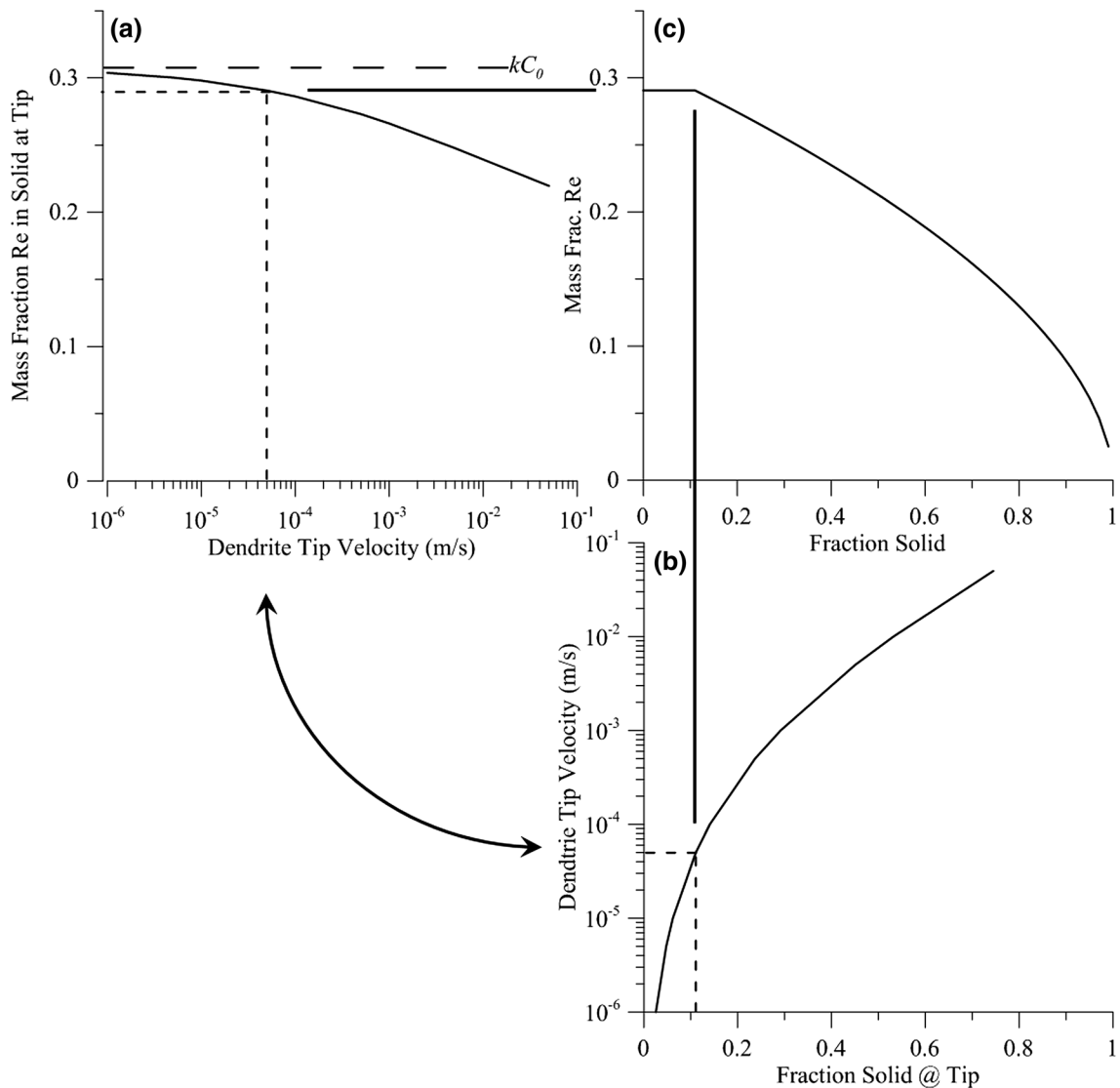
Fig. C1—Three plots: (*a*) dendrite tip solid composition *vs* dendrite tip velocity, (*b*) fraction solid at the tip *vs* velocity and (*c*) the microsegregation profile, solid composition *vs* fraction solid for the truncated Scheil model for $V = 5 \times 10^{-5}$ m/s. The arc connects common values of the velocity on the two graphs. Note the flat composition profile in (c) at small values of fraction solid.

Table C1. Materials Parameters for Dendrite Tip Calculation

C_0 (Pct Re)	20
k	1.54
m_L (°C/Pct)	3.85
D_L (m^2/s)	3E$-$9
$T_M\Gamma$ (km)	3.65E$-$7

solid composition *vs* fraction solid for the truncated Scheil model. Calculations are for the materials parameters in Table C1. Estimate of the solidification velocity is obtained using the expression, $V = \ell\dot{T}/(L/C)$, where ℓ is a characteristic size of the casting (3 mm), $\dot{T}$ is the

estimated cooling rate (10 K/s) and (L/C) is the ratio of heat of fusion to the heat capacity of Ni (666 K). This estimate yields a velocity of $\approx 5 \times 10^{-5}$ m/s, and gives a dendrite tip fraction solid of 0.11. This value roughly corresponds to the fraction solid width of the plateau seen at the start of the microsegregation profiles seen in Figure 6(c) and fraction solid width of the peak in Figure B1.

REFERENCES

1. N. Saunders and A.P. Miodownik: *CALPHAD (Calculation of Phase Diagrams): A Comprehensive Guide*, Pergamon, Oxford, 1998.
2. S.B. Maisel, N. Schindzielorz, A. Mottura, R.C. Reed, and S. Müller: *Phys. Rev. B*, 2014, vol. 90, p. 094110.
3. R.P. Elliott: *Constitution of Binary Alloys, First Supplement*, McGraw-Hill, New York, 1965, pp. 666–67.

4. S.A. Pogodin and M.A. Skryabina: *Izv. Sektora Fiz.-Khim. Analiza, Inst. Obshch. i Neorgan. Khim., Akad. Nauk. SSSR*, 1954, vol. 25, pp. 81–88.
5. T.B. Massalski: *Binary Alloy Phase Diagrams*, ASM International, Materials Park, 1990.
6. A. Nash and P. Nash: *Bull. Alloy Phase Diagr.*, 1985, vol. 6, pp. 348–50.
7. H. Okamoto: J. Phase Equilibria, 1992, vol. 13, p. 335. Also H. Okamoto: J. Phase Equilibria Diffus., 2012, vol. 33, p. 346.
8. E.M. Savitskii, M.A. Tylkina, and E.P. Arskaya: *Izv. Vuz. Tsvetn. Met.*, 1970, vol. 4, pp. 113–16.
9. C.M. Neubauer, D. Mari, and D.C. Dunand: *Scr. Metall. Mater.*, 1994, vol. 31, pp. 99–104.
10. S. Narita: Master's thesis, Graduate School of Hokkaido University, 2003.
11. S. Saito, T. Takashima, K. Miyama, K. Kurokawa, and T. Narita: *Mater. Trans.*, 2012, vol. 53, pp. 1078–83.
12. W.J. Boettinger, M.E. Williams, K.-W. Moon, G.B. McFadden, P.N. Patrone, and J.H. Perepezko: *J. Phase Equilibria Diffus.*, 2017, vol. 38, pp. 750–63.
13. K. Yaqoob and J.-M. Joubert: *J. Solid State Chem.*, 2012, vol. 196, pp. 320–25.
14. W. Huang and Y.A. Chang: *Mater. Sci. Eng. A*, 1999, vol. 259, pp. 110–19.
15. Automated Flow for Materials Discovery: http://www.aflowlib.org/. Accessed 6 Oct 2016.
16. Open Quantum Materials Database: http://oqmd.org/. Accessed 6 Oct 2016.
17. The Materials Project: https://www.materialsproject.org/. Accessed 6 Oct 2016.
18. H.W. Kerr and W. Kurz: *Int. Mater. Rev.*, 1996, vol. 41, pp. 129–64.
19. W.J. Boettinger, U.R. Kattner, K.-W. Moon, and J.H. Perepezko: NIST Special Publication 960-15. November 2006. https://www.nist.gov/publications/nist-recommended-practice-guides.
20. M. Hillert: *Phase Equilibria, Phase Diagrams and Phase Transformations: Their Thermodynamic Basis*, 2nd ed., Cambridge University Press, Cambridge, 2008, p. 244.
21. A.T. Dinsdale: *CALPHAD*, 1991, vol. 15, pp. 317–425.
22. A.D. Pelton and W.T. Thompson: *Prog. Solid State Chem.*, 1975, vol. vol. 10(part 3), pp. 119–55.
23. C.E. Campbell: NIST, unpublished research, 2016.
24. W.J. Boettinger and J.A. Warren: *Metall. Mater. Trans. A*, 1996, vol. 27A, pp. 657–69.
25. W.J. Boettinger: J. Phase Equilibria Diffus., 2016, vol. 37, pp. 4–18. See also W.J. Boettinger, S.R. Coriell, and R.K. Trivedi: *Rapid Solidification Processing: Principles and Technologies IV*, R. Mehrabian and P. A. Parrish, eds., Claitor's Publishing Division, Baton Rouge, LA, 1988, pp. 13–25.
26. S.C. Flood and J.D. Hunt: *Appl. Sci. Res.*, 1987, vol. 44, pp. 27–42.